UC Davis
UC Davis Previously Published Works

Title

Elastically-homogeneous lattice models of damage in geomaterials

Permalink

https://escholarship.org/uc/item/4bz0v5j4

Authors

Asahina, Daisuke
Aoyagi, Kazuhei
Kim, Kunhwi
et al.

Publication Date

2017

DOI

10.1016/j.compgeo.2016.08.015

Peer reviewed

Research Paper

Elastically-homogeneous lattice models of damage in geomaterials

Daisuke Asahina [a,*], Kazuhei Aoyagi [b], Kunhwi Kim [c], Jens T. Birkholzer [c], John E. Bolander [d]

[a] Geological Survey of Japan, National Institute of Advanced Industrial Science and Technology (AIST), Higashi 1-1-1, Central 7, Tsukuba, Ibaraki 305-8567, Japan
[b] Horonobe Underground Research Department, Sector of Decommissioning and Radioactive Wastes Management, Japan Atomic Energy Agency (JAEA), Hokkaido, Japan
[c] Earth & Environmental Sciences Area, Lawrence Berkeley National Laboratory (LBNL), 1 Cyclotron Road, Berkeley, CA 94720, USA
[d] Department of Civil and Environmental Engineering, University of California, Davis, One Shields Avenue, Davis, CA 95616, USA

ABSTRACT

This study involves the development of the auxiliary stress approach for producing elastically-homogeneous lattice models of damage in geomaterials. The lattice models are based on random, three-dimensional assemblages of rigid-body-spring elements. Unlike conventional lattice or particle models, the elastic constants of a material (e.g., Young's modulus and Poisson's ratio) are represented properly in both global and local senses, without any need for calibration. The proposed approach is demonstrated and validated through analyses of homogeneous and heterogeneous systems under uni- and tri-axial loading conditions. Comparisons are made with analytical solutions and finite element results. Thereafter, the model is used to simulate a series of standard laboratory tests: (a) split-cylinder tests, and (b) uniaxial compressive tests of sedimentary rocks at the Horonobe Underground Research Laboratory in Hokkaido, Japan. Model inputs are based on physical quantities measured in the experiments. The simulation results agree well with the experimental results in terms of pre-peak stress-strain/displacement responses, strength measurements, and failure patterns.

© 2016 Elsevier Ltd. All rights reserved.

1. Introduction

Discrete modeling approaches have been used to study the elasticity and failure behavior of a variety of geomaterials, such as rock and concrete. Lattice models and particle-based models can be categorized as discrete modeling approaches, in which two-node, unidirectional elements interconnect neighboring nodes [11,17,30,12,15]. The use of primitive, two-node elements simplifies fracture modeling in that only two nodes are involved in the local process of material separation.

Due to the use of unidirectional elements, however, such models are inherently limited in their abilities to represent the stress-strain behavior of a continuum. A macroscopic representation of the elastic constants (e.g., Young's modulus and Poisson's ratio) is obtainable by adjusting the stiffness properties of the elements [28,10,25]. For lattices with irregular geometries, such macroscopic representations typically require calibration with laboratory tests. Optimization techniques have been developed to reduce calibration efforts [33].

The inability of lattice models to represent elasticity in a local sense is less appreciated [31,3]. Discrepancies with elastic continua appear in both regular and irregular lattice models. Various remedies have been proposed [29,16,8,19,13]. In some cases, the lattice nodes and elements directly correspond to material structure [5,12], such that local representation of elasticity is not a modeling objective. For irregular lattice representations of homogeneity (including homogeneous regions within heterogeneous media), however, such discrepancies depend on lattice geometry, which can be viewed as a spurious form of heterogeneity. Although the effective (i.e., macroscopic) elastic constants are represented, the material model is no longer elastically homogeneous in a local sense. Such spurious heterogeneity lacks physical bases and its influence on crack initiation and propagation is difficult to interpret. Elastically-homogeneous models are necessary for controlling the introduction of heterogeneity and its effects on fracture.

This research involves the development of elastically-homogeneous 3D lattice models and their application to simulating brittle failure of geomaterials. The model formulation relies on the auxiliary (or fictitious) stress approach, which was originally proposed for the elastic analyses of planar, regular triangle lattices [3]. Herein, the approach is extended for use in random, three-dimensional assemblages of rigid-body-spring elements, which are a form of lattice model. Capabilities of the model are demonstrated through comparisons with theory (for homogeneous

* Corresponding author.
 E-mail address: d-asahina@aist.go.jp (D. Asahina).

systems) and with finite element results (for heterogeneous systems). In particular, the proposed model is capable of representing elastic continua both globally and in a local sense without the introduction of free parameters. The inability of conventional lattice models to represent local stress-strain conditions is presented for comparison. The ability to represent tensile softening, including local control of fracture energy along the crack path, is also demonstrated.

The proposed model is used to simulate a series of experiments conducted by the Japan Atomic Energy Agency (JAEA) at the Horonobe Underground Research Laboratory (URL) in Hokkaido, Japan [20,21]. The experiments include split-cylinder tests and uniaxial (unconfined) compression tests on sedimentary rock specimens taken from core samples. One set of model inputs is used to simulate both forms of testing. In general, the loading branches, peak loads, and failure patterns produced by the model agree well with the experimental results. For the unconfined compression test simulations, inclinations of the damage plane are well-defined and in agreement with theory.

2. Model framework

The elasticity and fracturing of geomaterials is modeled using a rigid-body-spring network, which is a special type of lattice model. The rigid-body-spring concept is briefly described in this section. Additional details of the model can be found elsewhere [9,2].

2.1. Domain discretization and model formulation

Domain discretization is based on the Delaunay/Voronoi dual tessellations of an unstructured set of nodal points placed within the domain. The Delaunay edges define the *i-j* connectivity of the lattice elements (Fig. 1); the Voronoi polygon associated with each Delaunay edge defines the cross-section of the respective element. For 3D case, each node has three translational and three rotational degrees of freedom. Element flexibility is lumped into a zero-size spring set, with local coordinate axes (n-s-t), located at the area centroid of the facet. The spring set is formed from three axial springs aligned with the local axes and having stiffness coefficients k_n, k_s, and k_t, respectively. The spring set also includes rotational springs about the same axes with stiffness coefficients, $k_{\varphi n}$, $k_{\varphi s}$, and $k_{\varphi t}$, respectively. In forming the element stiffness matrix, displacement jumps associated with each spring are related to the nodal degrees of freedom through rigid-body constraints [24]. Element matrices are assembled to form the system equilibrium equations in the conventional manner.
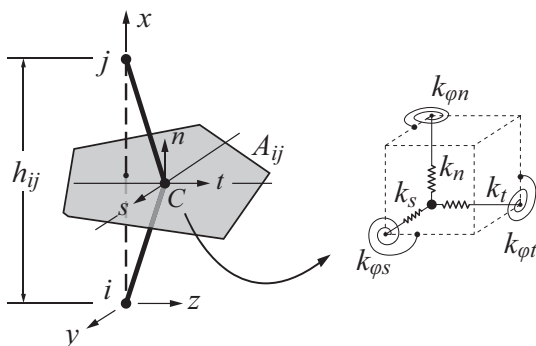

Fig. 1. Typical lattice element defined by nodal connectivity *i-j* and the Voronoi facet associated with the two nodes. A zero-size spring set, using local coordinate axes *n-s-t*, is located at centroid *C* of facet area A_{ij}.

The stiffness coefficients are assigned according to

$$k_s = k_t = \alpha_1 k_n = \alpha_1 \alpha_2 E \frac{A_{ij}}{h_{ij}}, \quad \text{and} \quad k_{\varphi n} = E \frac{J_p}{h_{ij}},$$

$$k_{\varphi s} = E \frac{I_{ss}}{h_{ij}}, \quad k_{\varphi t} = E \frac{I_{tt}}{h_{ij}} \tag{1}$$

in which E is Young's modulus, h_{ij} is the distance between nodes i and j, and A_{ij} is the area of the Voronoi polygon associated with nodes i and j. J_p, I_{ss}, and I_{tt} are the polar and two principal moments of inertia, respectively, of the Voronoi polygon with respect to its area centroid. By adjusting α_1 and α_2 in accordance with experimental results, the elastic constants E and v can be represented in a macroscopic sense. When $\alpha_1 = \alpha_2 = 1$, which corresponds to $v = 0$, the model is elastically homogeneous [6]. As one of the main contributions of this work, an approach for accurately realizing $v \neq 0$ (in both macroscopic and local senses) is presented in Section 3.

2.2. Nodal stress calculation

Nodal stress calculations are based on the spring-set forces of each lattice element framing into a particular node (Fig. 2a). The spring-set forces are calculated from the nodal displacements and the element stiffnesses. For an arbitrary cross-section of the Voronoi cell through the corresponding lattice node, local force components F_n, F_s, and F_t can be calculated to satisfy the force equilibrium (Fig. 2b). Within these equilibrium calculations, the force contributions of facets intersected by the cross-section plane are weighted. The corresponding stress components σ_n, σ_s, and σ_t are obtained by dividing F_n, F_s, and F_t, respectively, by the cross-section area. Repeating this exercise for three mutually orthogonal cross-sections, the nodal state of stress is determined. Details are given by Yip et al. [32]. The ability to calculate tensorial measures of stress at the lattice nodes is an integral part of the methods and analyses presented in the following sections.

2.3. Fracture criterion

Lattice models based on the rigid-body-spring concept have been used to model fracture driven by predominately tensile loading [6]. For a typical element within an irregular lattice, the loading direction does not generally align with the facet-normal direction (Fig. 2a). The resultant of the set of forces, $F_R = \left(F_n^2 + F_s^2 + F_t^2\right)^{0.5}$, is used to obtain a measure of stress, σ_R, which is defined as

$$\sigma_R = F_R / A_{ij}^P \tag{2}$$

where A_{ij}^P is the projection of the facet area on a plane perpendicular to the direction of F_R. For each element within the model, σ_R is compared with the cohesive stress, which varies according to a prescribed function of the crack opening displacement [6].

Alternatively, a Mohr-Coulomb criterion can be used to define failure conditions. The vectorial stresses associated with the individual spring sets are compared with the Mohr-Coulomb surface. This approach has physical bases when the element orientations are related to material features, such as the matrix-inclusion interface in composite materials [26]. Otherwise, however, randomly positioned elements do not correspond to actual material features and the physical interpretation of the Mohr-Coulomb parameters is less clear.

For the simulations presented in Section 5, the nodal stress tensor is used as an alternative basis for fracture modeling [4]. Intra-element stress values are calculated using

$$\bar{\boldsymbol{\sigma}} = (\boldsymbol{\sigma}_i + \boldsymbol{\sigma}_j)/2 \tag{3}$$

where $\boldsymbol{\sigma}_i$ and $\boldsymbol{\sigma}_j$ are the stress tensors at neighboring nodes, i and j, respectively. The stress state for each element can be represented
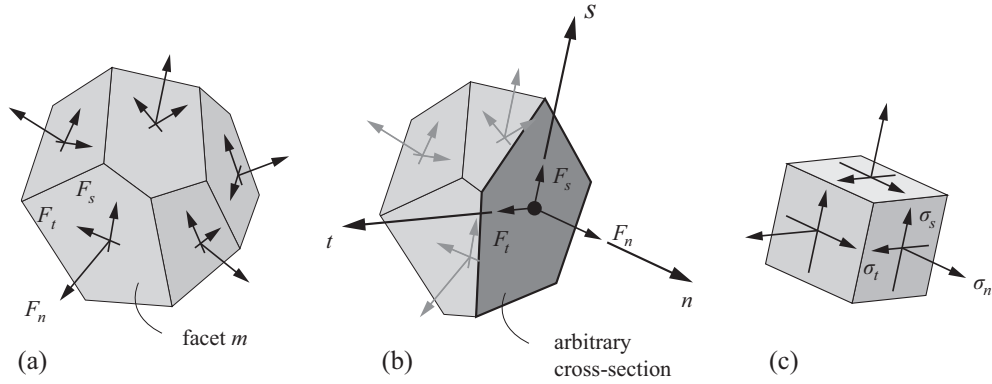
Fig. 2. (a) Element spring-set forces acting on the facets of a Voronoi cell, (b) calculated forces acting on an arbitrary cross-section through the associated lattice node, and (c) material element representation of the stress state at the lattice node.

by a Mohr's circle format based on $\bar{\sigma}$, and compared with a Mohr-Coulomb surface with a tension cutoff. This approach of fracture definition is less sensitive to mesh configuration, since it relies on stress measures that are relatively independent of element geometry and orientation.

3. Auxiliary stress approach for 3D irregular lattices

The basic concept of the auxiliary (or fictitious) stress approach has been described in a previous study [3], for the special case of planar lattices composed of regular triangles. The extension to 3D irregular lattices, described herein, involves several generalizations. The formulation is presented as a series of steps.

Step 1: Nodal displacements are determined for the prescribed boundary conditions by solving the system equations for the case of $\alpha_1 = \alpha_2 = 1$ in Eq. (1), which corresponds to $v = 0$. As shown in previous work [6], this condition provides an elastically homogeneous basis for introducing the Poisson effect. Principal stresses, σ_1, σ_2, and σ_3, and principal strains, ε_1, ε_2, and ε_3, are calculated at each node using the method for nodal stress calculation given in Section 2.2. The indices 1, 2, and 3 denote the maximum, intermediate, or minimum principal values, respectively.

Step 2: At each node, an auxiliary measure of orthogonal strain is determined using the vector form of the principal strains, $\varepsilon_P = [\varepsilon_1 \ \varepsilon_2 \ \varepsilon_3]^T$, and actual non-zero value of v

$$\boldsymbol{\varepsilon}' = v\hat{\mathbf{I}}\boldsymbol{\varepsilon}_P \tag{4}$$

in which

$$\hat{\mathbf{I}} = \begin{bmatrix} 0 & 1 & 1 \\ 1 & 0 & 1 \\ 1 & 1 & 0 \end{bmatrix}. \tag{5}$$

The auxiliary stress is obtained by multiplying both sides of Eq. (4) by E

$$\boldsymbol{\sigma}' = Ev\hat{\mathbf{I}}\boldsymbol{\varepsilon}_P = v\hat{\mathbf{I}}\boldsymbol{\sigma}_P \tag{6}$$

where $\boldsymbol{\sigma}_P = [\sigma_1 \ \sigma_2 \ \sigma_3]^T$.

Step 3: Auxiliary stress is introduced into the lattice elements framing into each node i via a set of tractions, which are applied to the facets of the associated Voronoi polyhedral cell (Fig. 3). For facet m, the traction vector is expressed by

$$\mathbf{t}_m^i = \mathbf{S}^i \mathbf{n}_m^i \tag{7}$$

where $\mathbf{S}^i = \mathbf{diag}(\sigma_1', \sigma_2', \sigma_3')$ for node i, and $\mathbf{n}_m^i$ is the outward unit normal vector of facet m from node i. To facilitate explanation,
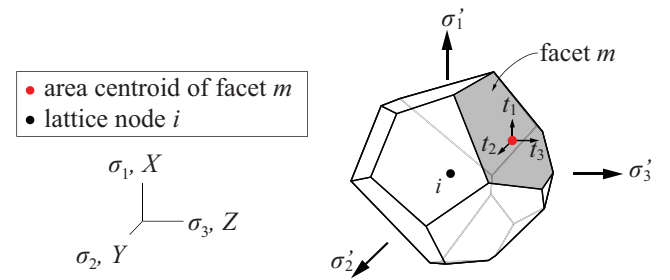

Fig. 3. Auxiliary stresses and associated traction vectors for facet m of Voronoi cell i.

but without loss of generality, the coordinate and principal directions in Fig. 3 are assumed to be aligned. The auxiliary force acting on facet m is then

$$\mathbf{f}_m^i = \mathbf{t}_m^i A_m \tag{8}$$

where A_m is the area of facet m. This auxiliary force, resolved into normal and tangential components, is introduced into the spring set of the rigid-body-spring element associated with the facet. The set of auxiliary forces acting on the cell facets is in equilibrium.

Step 4: The introduction of auxiliary spring forces produces nodal displacements, in accordance with the prescribed boundary conditions of Step 1. The nodal displacements are obtained from the system equations by a conventional back-substitution algorithm, which is not computationally burdensome. The new principal stresses, $\hat{\boldsymbol{\sigma}}_P = [\hat{\sigma}_1 \ \hat{\sigma}_2 \ \hat{\sigma}_3]^T$, are calculated at each nodal site.

Step 5: Convergence of the algorithm is achieved when $\|\hat{\boldsymbol{\sigma}}_P - \boldsymbol{\sigma}_P\| < e$, where $\|\cdot\|$ is the Euclidean norm with respect to all nodal values and e is a predefined tolerance. Otherwise, the procedure returns to Step 2 with updated $\boldsymbol{\sigma}_P = \hat{\boldsymbol{\sigma}}_P$.

Several analysis methods use additional force terms associated with particle interactions within some spatial distance, e.g., the embedded-atom model [14] and smooth particle hydrodynamics [27]. These forces depend on the electron density or some other quantity about each particle to simulate elastic continua, as well as large deformation behavior. On the other hand, the auxiliary forces utilized in this study are based on tensorial representations of stress at each node, which are derived from nearest-neighbor interactions. Nearest-neighbors are defined by the Delaunay tessellation of the set of nodal points.

Iteration is typically required for problems with general boundary conditions or when modeling heterogeneous systems.

Convergence is ensured since the auxiliary stresses of Eq. (6) become progressively smaller for the normal range of v. For some special cases, however, iteration is not required. These cases include prismatic volumes of homogeneous materials under uniform displacements applied along the boundaries in one or more coordinate directions (Fig. 4a). Asahina et al. [3] derived asymptotic values of the auxiliary stress, such that iteration is not necessary, for planar cases. Herein, the derivation is extended to three dimensions. Under imposed boundary displacements, as shown in Fig. 4a, the auxiliary forces for each iteration $j = 2, 3, \ldots, n$, are

$$\boldsymbol{\sigma}'^{(j)} = v\hat{\mathbf{I}}\boldsymbol{\sigma}'^{(j-1)} \tag{9}$$

where $\boldsymbol{\sigma}'^{(1)} = v\mathbf{I}\boldsymbol{\sigma}_P$. The cumulative effect of the iteration process can be expressed as

$$\boldsymbol{\sigma}' = \sum_{k=1}^{n} \boldsymbol{\sigma}'^{(k)} \tag{10}$$

Substituting Eq. (9) into Eq. (10), asymptotic values of the auxiliary stresses are obtained

$$\boldsymbol{\sigma}' = \begin{bmatrix} \sum_{k=1}^{\infty} J'_k v^k & \sum_{k=1}^{\infty} J_k v^k & \sum_{k=1}^{\infty} J_k v^k \\ \sum_{k=1}^{\infty} J_k v^k & \sum_{k=1}^{\infty} J'_k v^k & \sum_{k=1}^{\infty} J_k v^k \\ \sum_{k=1}^{\infty} J_k v^k & \sum_{k=1}^{\infty} J_k v^k & \sum_{k=1}^{\infty} J'_k v^k \end{bmatrix} \boldsymbol{\sigma}_P \tag{11}$$

where J_k stands for the k th Jacobsthal number, $J_k = J_{k-1} + 2J_{k-2}$, starting with $J_0 = 0$ and $J_1 = 1$. J'_k is defined as $J'_k = J_k + (-1)^k$.

To demonstrate the application of Eq. (11), consider a cubic cell under imposed boundary displacements, $\delta_X = -\delta/2$, $\delta_Y = \delta/3$, and $\delta_Z = -\delta$ (Fig. 4a). Note that tensile stress is positive. Absolute differences between the exact and computed values of principal stresses, for different values of Poisson's ratio, are shown in Fig. 4b. The magnitude of σ_3 is used as a normalizing factor. As expected, faster convergence to the exact solution is observed with lower Poisson's ratio. For $v \leqslant 0.2$, reasonable accuracy can be achieved with four or five iterations. For the numerical examples presented in the following sections, four and twenty iterations are conducted to compute stresses for $v \leqslant 0.2$ and $v = 0.4$, respectively.

4. Validation exercises

4.1. Elastic uniformity

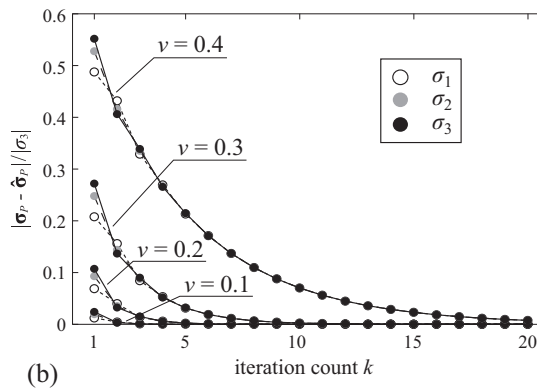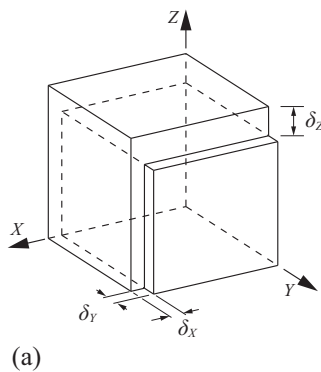The accuracy of the auxiliary stress approach, employed within in 3D irregular lattices, is demonstrated through the following exercises. Consider a cubic volume of an elastic, isotropic material subjected to either uniaxial or triaxial loading, as shown in Fig. 5. Although the domain contains a spherical inclusion (Fig. 5b and c), it can be rendered homogeneous by assigning the same set of material properties to both the inclusion and surrounding matrix. Discretization of the matrix-inclusion boundary and mesh size gradation are controlled by the spatial positioning of generator points for the Voronoi diagram. Comparisons are made in terms of nodal displacement, nodal stress, and elemental stress.

4.1.1. Homogeneous systems: triaxial loading

The domain of Fig. 5 is rendered homogeneous by assigning the same material properties to both the matrix and inclusion. The displacement boundary conditions depicted in Fig. 4a are employed with $\delta_X = -\delta/2$, $\delta_Y = \delta/3$, and $\delta_Z = -\delta$. Results of the auxiliary stress approach are examined for two different sets of spring constants (α_1 and α_2 in Eq. (1)), as indicated in Table 1. The case of $v = 0.4$ is presented to demonstrate capabilities of the approach for Poisson ratios outside the range accommodated by conventional lattice models. In addition, the conventional lattice is examined for: (i) $\alpha_1 = \alpha_2 = 1$, which provides $v = 0$; and (ii) $\alpha_1 = 0.32$ and $\alpha_2 = 1.56$, which provides a macroscopic Poisson ratio of $v = 0.17$. Relative error of the nodal displacements for each case are given in Table 1, where relative error is defined as

$$e_r = \frac{\|u - u^h\|_2}{\|u\|_2}, \quad \|u - u^h\|_2 = \sqrt{\sum_{i=1}^{N} (u(\mathbf{X}_i) - u^h(\mathbf{X}_i))^2}, \tag{12}$$

in which $\| \cdot \|_2$ is the L_2 error norm; u and u^h are the exact and numerical solutions, respectively, in each direction at locations X; and N is the total number of nodes. Results presented in the table agree well with theory, except for the macroscopic representation of $v = 0.17$ with the conventional lattice approach.

Fig. 6 shows the Mohr circle representation of stress state at each of the internal nodes, as provided by the nodal stress tensor calculations for a particular inclination, $\psi = 0-2\pi$ with an interval of $\pi/18$, about each of the three principal directions. For the case of $v = 0$, the results accurately represent the state of stress at all nodes. There is no evidence of bias due to mesh size, which is strongly graded, or semi-random mesh geometry. When $v \neq 0$, however, the conventional approach exhibits much scatter about the theoretical solution. The auxiliary stress approach is accurate for $v \geqslant 0$, including v values outside the range accommodated by conventional lattice models. The influence of Poisson's ratio on the stress state is evident: the major principal stress moves from the tensile to compressive regime with increasing v.

Fig. 4. (a) Prescribed triaxial loading, and (b) the absolute differences between the exact stress values and those calculated by Eq. (11) for different values of Poisson's ratio.
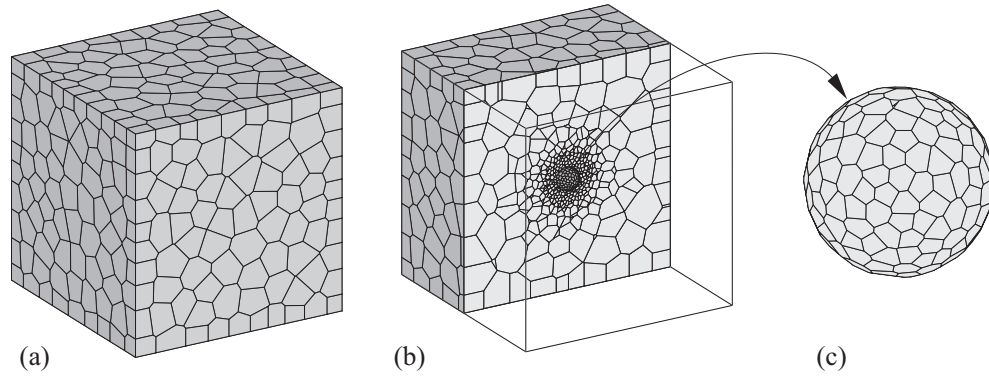
Fig. 5. (a) Domain discretization based on the Voronoi tessellation of a semi-random set of points; (b) cross-section through spherical inclusion; and (c) enlarged view of inclusion.

Table 1
Relative errors e_r in displacements for triaxial loading.

Poisson ratio, v	0.0	0.17	0.17	0.4
Coefficients of Eq. (1)	$\alpha_1 = \alpha_2 = 1$	$\alpha_1 = 0.32$, $\alpha_2 = 1.56$	$\alpha_1 = \alpha_2 = 1$	$\alpha_1 = \alpha_2 = 1$
Auxiliary stresses introduced	No (conventional approach)	No (conventional approach)	Yes	Yes
X-axis values	4.65×10^{-8}	8.76×10^{-3}	3.24×10^{-8}	5.47×10^{-8}
Y-axis values	6.48×10^{-8}	3.53×10^{-2}	2.49×10^{-8}	1.47×10^{-7}
Z-axis values	2.94×10^{-8}	1.21×10^{-2}	3.14×10^{-8}	6.91×10^{-8}

4.1.2. Homogeneous systems: uniaxial loading

Fig. 7 shows the vectorial stress pair results for all elements in the homogeneous system for $v = 0.17$. The lattice is under uniaxial compression due to vertical displacement, δ, imposed on the top layer of nodes without lateral restraint. The stress pair can be calculated from the spring forces acting in the rigid-body-spring (lattice) element divided by area, A_{ij}, of the corresponding Voronoi facet (Fig. 1). The full set of results has been plotted in the n-ρ plane, where $\sigma_\rho = (\sigma_s^2 + \sigma_t^2)^{0.5}$. The stress pairs of the proposed approach form a semi-circle in σ_n-σ_ρ stress space, in accordance with the theory, whereas results from conventional lattice model exhibit much scatter.

For a different perspective, Fig. 8 plots the normal stress acting in all elements versus the element orientation, θ_Z, with respect to the loading direction. The auxiliary stress approach provides a smooth, single-line transition between $\sigma_n = E\delta/L$ for $\theta_Z = 0$ and $\sigma_n = 0$ for $\theta_Z = \pi/2$, in accordance with theory. In contrast, a large amount of scatter appears for the conventional lattice model. For higher θ_Z, elements in the conventional model exhibit tension, which is theoretically inadmissible. These discrepancies of the conventional lattice model, seen in both Figs. 7 and 8, could lead to erroneous crack initiation and propagation when using a stress based fracture criterion.

4.1.3. Heterogeneous systems: uniaxial loading

The discretization presented in Fig. 5 is kept, but the modular ratio of the inclusion and matrix phases is assumed to be $E_i/E_m = 3$; the Poisson ratio is assumed to be either $v = 0$, or $v = 0.17$, for both phases. Figs. 9 and 10 show contour diagrams of principal tensile stress on the central section through the inclusion for each respective value of v. The normalizing factor, $\sigma = E_m\delta/L$, is used in both figures. Each figure also presents results based on constant strain tetrahedral (four-node) finite elements, which conform to the same Delaunay tessellation that defines the lattice topology. As the 3D model domain is symmetric, only the half of the cross section is shown for each analysis case.

The good agreement between the lattice model and the finite element method (FEM), for both $v = 0$ and $v = 0.17$, serves to validate the auxiliary stress approach. The Poisson effect significantly influences the stress conditions around the stiff inclusion. The
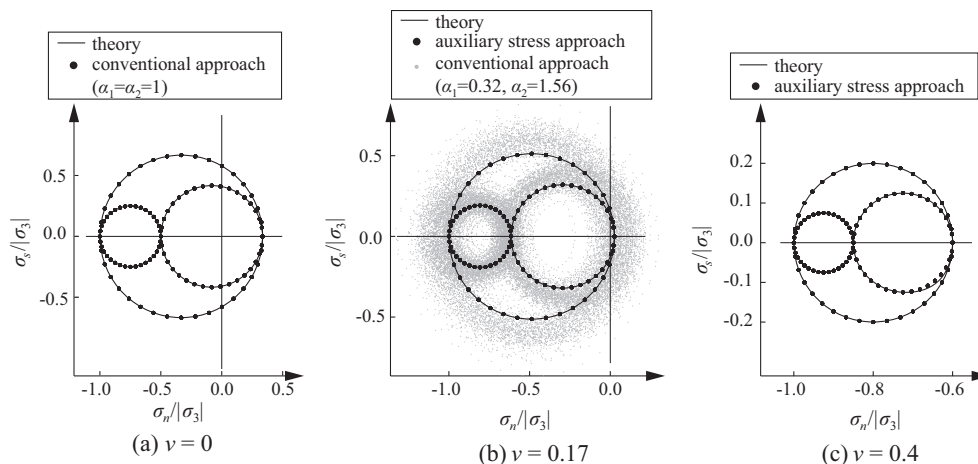

Fig. 6. Mohr's circle representation of 3D stress state at the lattice nodes: (a) $v = 0$, (b) $v = 0.17$, and (c) $v = 0.4$. The conventional approach is unable to simulate the case of $v = 0.4$ and therefore results are not shown.
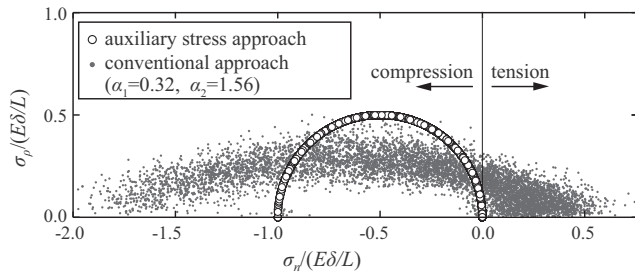
Fig. 7. Elemental stresses due to uniaxial compressive loading ($v = 0.17$).

results are similar to those obtained with planar regular lattices in Asahina et al. [3].

4.2. Fracture of homogeneous media under uniaxial tension

A utility of the auxiliary stress approach is demonstrated by simulating tensile softening of a homogeneous material. This basic case is relevant for a range of practical problems, including those related to fracture induced by volumetric instabilities associated with drying. Consider the case of a square panel subjected to uniaxial tension, as shown in Fig. 11a. Load is applied by displacement control. Roller supports act along the loaded edges of the lattice to allow for free contraction due to the Poisson effect. In the following analyses, results of the proposed approach for $v = 0.17$ are compared with those based on $\alpha_1 = \alpha_2 = 1$ for $v = 0$.

Fig. 11b shows the tension-softening relation employed for each element spring-set. The two parameters ($\beta = 0.2$, $\eta = 0.25$) define the break point in the relation. Fracture is governed by the first of the approaches described in Section 2.3 (i.e., a vectorial measures of stress, according to Eq. (2), is compared with the residual stress based on the softening relation). After fracture initiation within an element, the auxiliary forces are no longer introduced for that element.

Here too, prior to cracking, relative errors of the nodal displacements (Eq. (12)) for the proposed approach are insignificant in both the vertical and lateral directions. For both the proposed approach and for $v = 0$ ($\alpha_1 = \alpha_2 = 1$), the elemental stress, σ_R (Eq. (2)), reaches the tensile strength in all elements simultaneously. Fig. 11c compares simulated load-displacement curves for the two cases. The results of the proposed approach agree well with those for $v = 0$ ($\alpha_1 = \alpha_2 = 1$), which match the theoretical result based on the element softening relation.

Each fracture event consumes an amount of energy within the corresponding equilibrium iteration. The local energy consumption, g_F, can be computed by summing such energy increments

throughout the load history [6]. Fig. 12 plots g_F, normalized by fracture energy G_F, alongside the simulated crack patterns. G_F is the area under the bilinear softening diagram shown in Fig. 11b. Each bar in the energy plots corresponds to a fractured element. Bar thickness corresponds to the projection of the element facet area on the vertical plane.

For both the proposed approach and for $v = 0$ ($\alpha_1 = \alpha_2 = 1$), fracture energy consumption is essentially uniform along the crack path (Fig. 12a and b) and in agreement with the theoretical value of $g_F/G_F = 1$. The approach is energy conserving and not appreciably affected by the irregular mesh pattern. Cracking occurs to the sides of the localized crack, but it is insignificant in terms of energy consumption. These results demonstrate the ability to simulate tension softening in conjunction with the proposed approach. Further developments are needed to simulate softening behavior under multiaxial loading conditions.

5. Rock test simulations

5.1. Experimental program

The Horonobe Underground Research Laboratory (URL) of the Japan Atomic Energy Agency (JAEA) has performed a series of laboratory scale experiments on sedimentary rocks [20,21,1]. The tests were conducted on rock core samples obtained from a borehole taken prior to construction of the URL and intended to provide basic data for the geomechanical conditions of the URL. In this paper, two standard mechanical tests are analyzed: (a) split-cylinder test (SCT) [22], and (b) uniaxial compression test (UCT) [7], as the objects of the simulations that follow. The core samples, 30 mm in diameter and 60 mm long, were taken from the Wakkanai Formation which is categorized as massive (thickness > 200 m) and lithologically homogeneous siliceous mudstones [21]. Table 2 summarizes the experimental results, which are averages values obtained from three specimens. Two sampling depths, 0–50 m and 250–300 m from the boundary between the Koetoi and Wakkanai Formations, are considered in this simulation. The tensile strength, f_t, and the uniaxial compressive strength, f_c, are obtained by SCT and UCT, respectively. The elastic constants (E, v) are measured from the initial linear part of stress-strain curves (i.e., from the origin to 50% of the uniaxial compressive strength obtained by UCT).

5.2. Numerical simulations

The split-cylinder test (SCT) and uniaxial compression test (UCT) of the sedimentary rocks are simulated using the 3D irregular lattice models to demonstrate their basic capabilities to
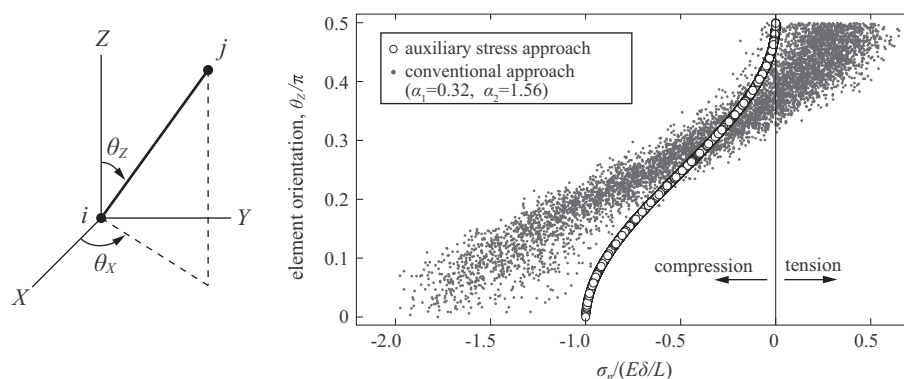

Fig. 8. Dependence of element normal stress on element orientation with respect to the loading direction ($v = 0.17$).

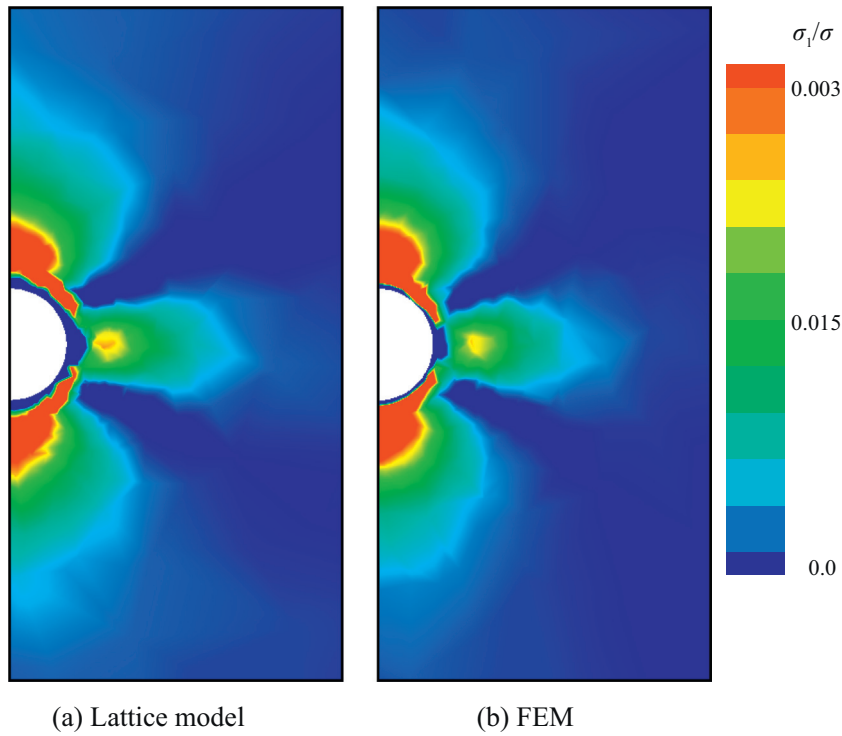(a) Lattice model   (b) FEM

Fig. 9. Principal tensile stress local to a stiff spherical inclusion within a cubic domain under applied uniaxial compressive strain ($v = 0$ for both phases): (a) lattice model using the auxiliary stress approach, and (b) finite element method (FEM).
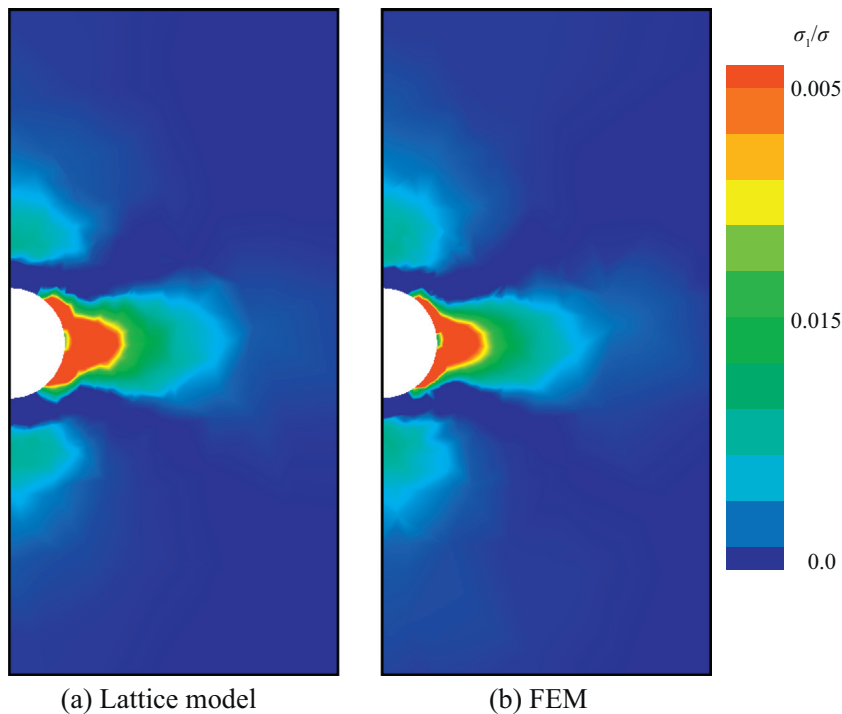

(a) Lattice model   (b) FEM

Fig. 10. Principal tensile stress local to a stiff spherical inclusion within a cubic domain under applied uniaxial compressive strain ($v = 0.17$ for both phases): (a) lattice model using the auxiliary stress approach, and (b) finite element method (FEM).

replicate pre-peak behavior and brittle failure patterns. Lattice models presented herein represent fracture as an even-by-event process, in which each event (i.e., the breaking of a single lattice element) is preceded by a linear elastic solution of the equilibrium equations [17]. For the results that follow, the auxiliary stress

approach, discussed in Section 3, is conducted within each solution cycle, such that the Poisson effect is properly represented within stress value calculations. The auxiliary forces are not introduced for the fractured elements. At this stage of model development, softening behavior and frictional effects are not simulated. Bulk
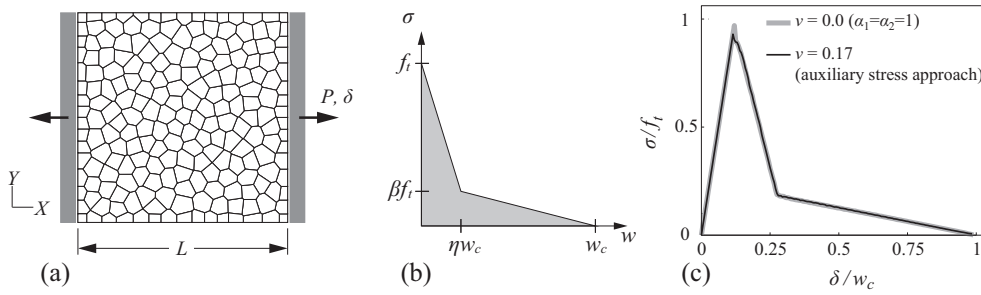
Fig. 11. Uniaxial tension test simulation: (a) homogeneous square panel, (b) post-peak softening relation for each element spring set, and (c) load-displacement response curves.
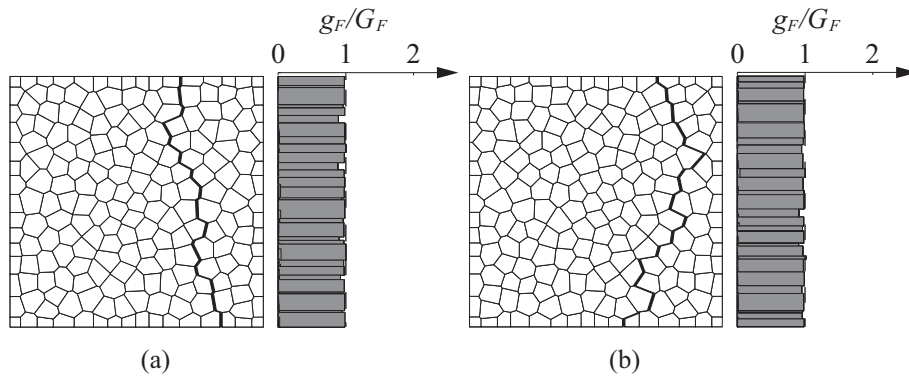

Fig. 12. Crack patterns and distributions of local fracture energy: (a) $v = 0.17$ (auxiliary stress approach), and (b) $v = 0$ ($\alpha_1 = \alpha_2 = 1$).

Table 2
Summary of the measured values by SCT and UCT at two sampling depths.

Sampling depth[a] [m]	Tensile strength, f_t [MPa]	Uniaxial compressive strength, f_c [MPa]	Young's modulus, E [MPa]	Poisson ratio, v
0–50	3.24	−25.1	2490	0.16
250–300	1.15	−11.0	1910	0.26

[a] From the boundary between the Koetoi and Wakkanai Formations.

material properties (E and v) presented in Table 2 are directly used for the parameters of the lattice elements through Eqs. (1) and (6), respectively, without any need for calibration. In the simulations, load is applied by displacement control and load rate/duration effects are not incorporated. Neither the friction of the loading platen nor the nonlinear contact conditions are considered.

5.2.1. Split-cylinder test (SCT)

The 3D lattice model, shown in Fig. 13a, represents the sedimentary rock sample within the split-cylinder test configuration. The mesh size is finer along the loading path and coarser in the lower stress regions where the lattice elements are not likely to approach the critical stress conditions. Arrays of nodes are positioned to represent the loading strip, by which the load was increased incrementally in the Y-direction until the specimen reached peak load. Since fracture in a SCT is mainly dominated by indirect tensile failure, the fracture criterion of the lattice elements depends on the major principal tensile stress, σ_1, and the tensile strength, f_t (Table 2).

For verification, analytical solutions are adopted [18], which estimate tensile and compressive stresses, $\sigma_{SCT,t}$ and $\sigma_{SCT,c}$, along the loaded diameter of the sample, i.e.,

$$\sigma_{SCT,t} = \frac{2P}{\pi bd}, \tag{13}$$

$$\sigma_{SCT,c} = \frac{2P}{\pi bd}\left(\frac{d^2}{r(d-r)} - 1\right) \tag{14}$$

where P is the applied load, and b and d are the length and diameter of the split-cylinder specimen, respectively; r is the vertical distance from a point to the applied load. Note that these equations are based on the assumption of a homogeneous and isotropic material. Fig. 13b shows normalized principal stresses at each of the nodes prior to peak load versus the nodal coordinate in loading direction (Y-direction). The figure also shows the computed stress results conform nicely to the theoretical stress limits. The finer mesh along the loading path causes the stress points to be denser nearby the theoretical lines. The ratio of $\sigma_1/\sigma_{SCT,t}$ to $\sigma_3/\sigma_{SCT,t}$ at the middle of the loading path is 3 in accordance with theory.

Fig. 14 compares experimental and simulated stress-displacement responses of the SCT specimen at the sampling depth of 0–50 m and 250–300 m from the boundary. The initial stage of the experimental responses shows hardening behavior that is typically associated with the nonlinear contact conditions between the cylinder and the load platens. In that sense, each response curve has been shifted horizontally so that a tangent to the linear portion passes through the origin. The averaged experimental strength, f_t, is indicated in each figure. The simulated and the experimental results agree well, with respect to both the slope of the curve and strength. Fig. 15 shows a typical fracture pattern of the cylinder specimen and a simulated fracture pattern, in which the broken elements are indicated by their respective Voronoi facets. Fracture initiates and propagates in the middle of the specimen along the loading path, where the highest tensile stress exists. As expected, the fracture pattern is more complicated close to the loading platens.

5.2.2. Uniaxial compression test (UCT)

For UCT, the strength properties of the lattice element are defined by a Mohr-Coulomb line. Table 3 presents the Mohr-Coulomb parameters, φ and c, which were estimated from
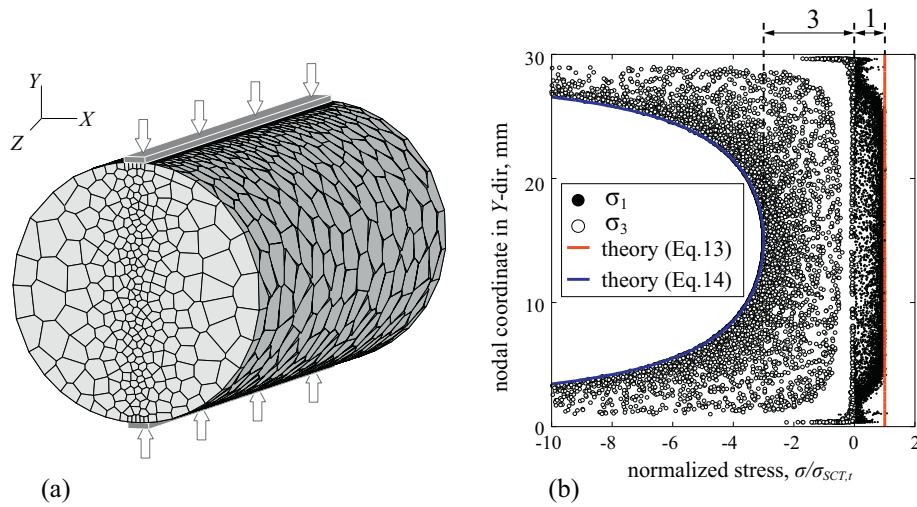
Fig. 13. (a) Voronoi discretization of the sedimentary rock specimen in the SCT configuration (≈15,000 nodes), and (b) normalized nodal stress and theoretical stress limits prior to peak load.
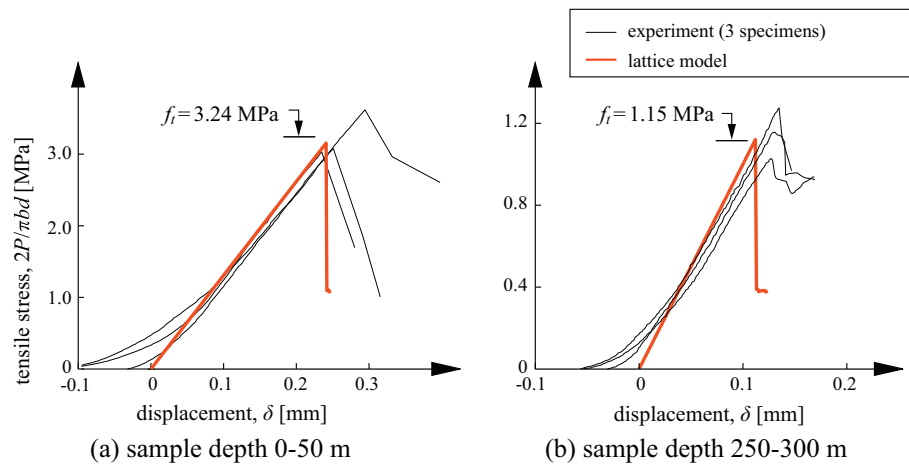

Fig. 14. Tensile stress-displacement response of SCT at the sampling depth of: (a) 0–50 m, (b) 250–300 m from the boundary. The average experimental strength, f_t, is indicated.
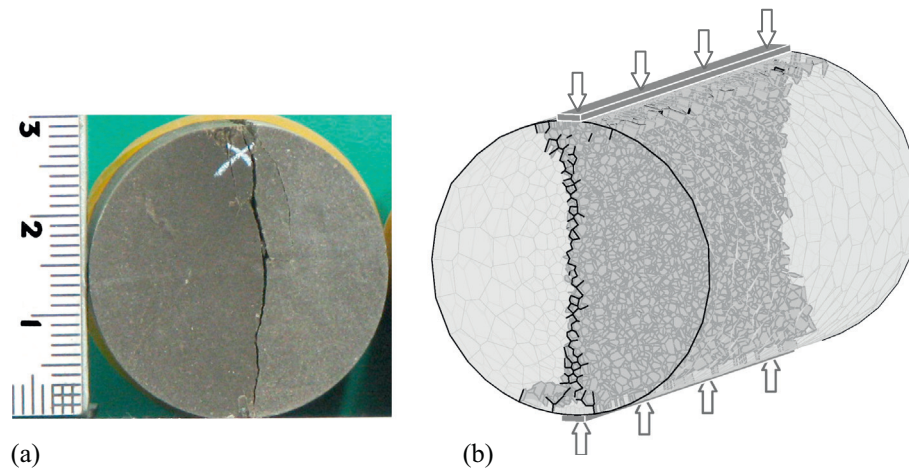

Fig. 15. SCT results: (a) typical failure pattern of SCT specimen, and (b) simulated failure pattern.

two sets of test results. For Set 1, as shown in Fig. 16, two parameters are calculated from the envelope curve that is tangent to the two stress circles using the strength values, f_t and f_c (Table 2). The

smaller and larger circles correspond to the critical stress conditions for SCT and UCT, respectively. The stress state of SCT is considered in the middle of the loading path, where the ratio
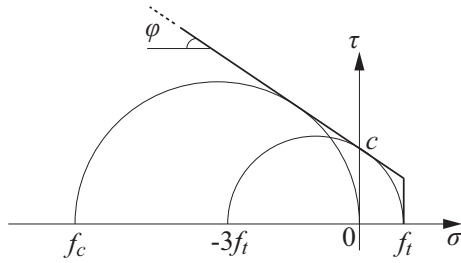
Fig. 16. Mohr-Coulomb line with tension cut-off determined by two strength values, f_t and f_c, measured by SCT and UCT, respectively.

of principal stresses in compression and tension is 3:1 (see Fig. 13b). For Set 2, the two parameters are estimated by a series of triaxial compression tests according to the method suggested by ISRM [23]. Fig. 17 shows the Mohr-Coulomb line and Mohr's circles for triaxial compression tests for two sampling depths. The Mohr-Coulomb lines are based on the relationship between the confinement pressure and the maximum axial stress of the triaxial compression tests [23,1].
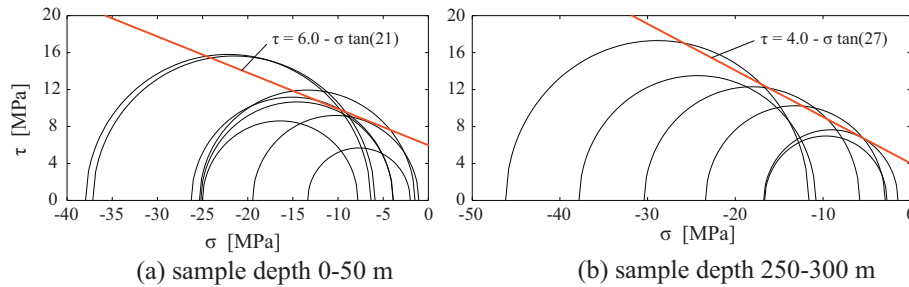
Fig. 18a shows a 3D discretization of the cylinder specimen subjected to uniaxial compression. The vertical displacements of the top and bottom layers of nodes are prescribed. Frictional resistance along the interface between the load platens and sample is not considered. Stress-strain curves are plotted in Fig. 18b and c for the samples at the depths of 0–50 m and 250–300 m from the boundary between the Koetoi and Wakkanai Formations, respectively. The axial stress is calculated from the total load applied at the top of cylinder and its cross-section area. The axial (vertical) strain, ε_v, is obtained from the relative displacement in the axial direction and the specimen height. The lateral strain, ε_h, is calculated as the average of six horizontal relative displacements divided by their respective gage lengths. These relative displacements are measured between sets of diametrically opposing nodes at heights of 10 mm, 30 mm, and 50 mm from the cylinder base. The macroscopic Poisson ratio is then $v_{eq} = -\varepsilon_h/\varepsilon_v$.

In the simulation, after the first element breakage neighboring elements undergo fracture even without increasing the load point displacement, signifying brittle failure. As seen in Fig. 18b and c, the model (based on the properties for Set 1) and experimental results agree along the loading branch of the stress-strain curves

Fig. 17. Mohr-Coulomb line based on Mohr's circles of triaxial compression tests at the sampling depths of: (a) 0–50 m, and (b) 250–300 m from the boundary. Adapted from Aoyagi et al. [1].
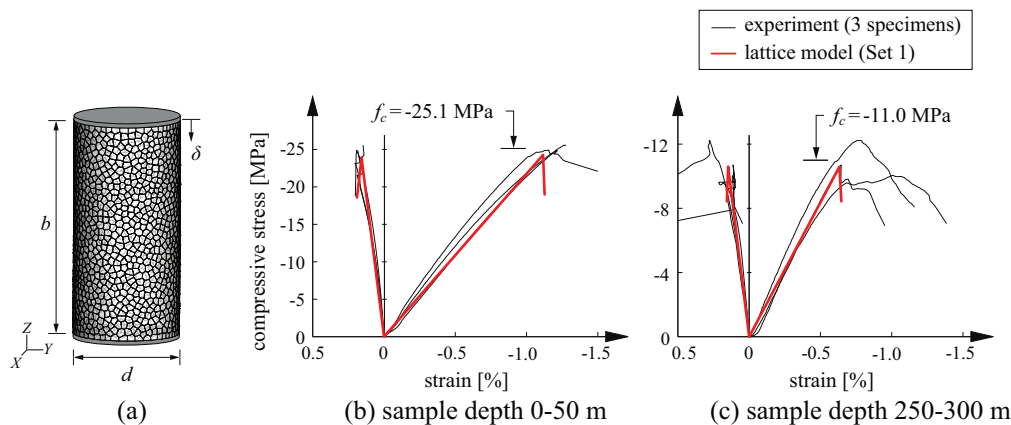

Fig. 18. Unconfined compression test: (a) Voronoi discretization of specimen (≈8800 nodes), and stress strain curves at sampling depths of: (b) 0–50 m, (c) 250–300 m from the boundary. The average experimental strength, f_c, is indicated.

Table 3
Two sets of strength properties used in the lattice model.

	Estimation method	Sampling depth[a] [m]	Internal friction angle, φ [°]	Cohesion, c [MPa]	# specimens	Correlation coefficient[b]
Set 1	SCT and UCT (Fig. 16)	0–50	41.3	5.76	3	–
		250–300	47.6	2.15	3	–
Set 2	Triaxial compression test (Fig. 17)	0–50	21.0	6.00	8	0.646
		250–300	27.0	4.00	6	0.968

[a] From the boundary between the Koetoi and Wakkanai Formations.
[b] The values are based on the maximum axial stress and the corresponding confining pressures.

Table 4
Compressive strength of UCT.

	Estimation method for φ and c	Sampling depth[a] [m]	Compressive strength of UCT [MPa]	
			Simulated results	$\sigma_{UCT,c}$ (Eq. (15))
Set 1	SCT and UCT (Fig. 16)	0–50	−24.3	−25.5
		250–300	−10.6	−11.1
Set 2	Triaxial compression test (Fig. 17)	0–50	−16.7	−17.5
		250–300	−12.5	−13.1

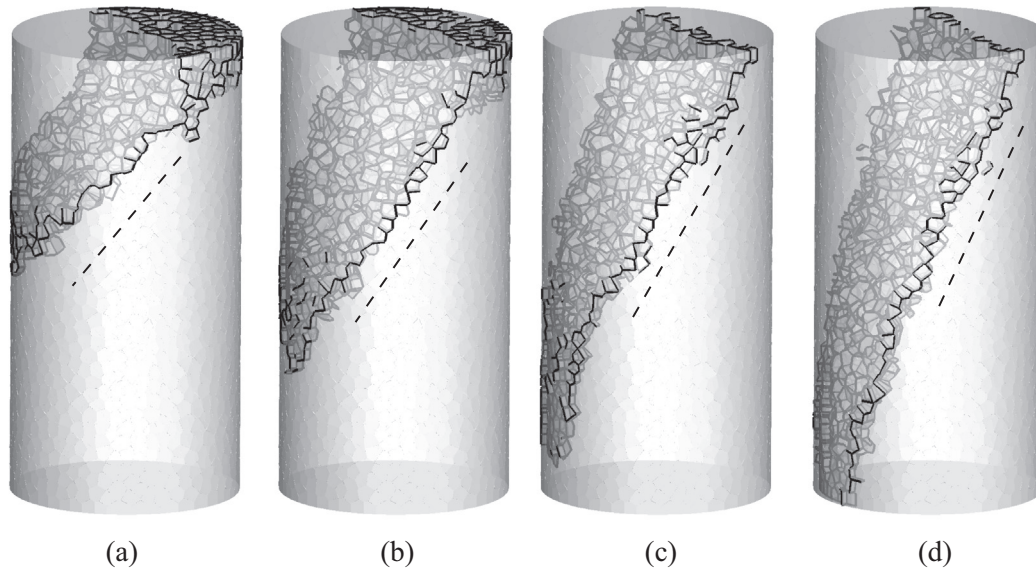[a] From the boundary between the Koetoi and Wakkanai Formations.

Fig. 19. Simulated fracture patterns for different internal friction angles φ: (a) 10°, (b) 20°, (c) 30°, and (d) 40°, with constant cohesion. The broken line in each figure indicates the critical plane angle, 45° + φ/2, according to theory.

and with respect to peak stress, although the mild pre-peak nonlinearity of the experimental results is not reproduced by the model. Table 4 compares the simulated and theoretical compressive strengths for both Sets 1 and 2. The uniaxial compressive strength, based on the Mohr-Coulomb parameters, φ and c (arranged in Table 3), can be obtained by the following theoretical formula [23]:

$$\sigma_{UCT,c} = -2c \cos \varphi / (1 - \sin \varphi) \tag{15}$$

As presented in Table 4, the peak stress values (i.e., uniaxial compressive strengths) obtained from the lattice models agree reasonably well with the theoretical values for all cases. The difference in compressive strengths between Sets 1 and 2 is due, in part, to the variation of the material properties and the influence of sampling depth at the Horonobe URL site, as discussed in [21]. The discrepancy becomes larger at the 0–50 m sampling depth, where a much lower correlation coefficient (see Table 3) has been observed nearby the boundary between the Koetoi and Wakkanai Formations [21,1]. The model presented here is elastically homogeneous due to use of the auxiliary stress approach. The lack of heterogeneity, either actual or artificial, contributes to the brittle behavior of model and affects the compressive strength estimates. It is anticipated that post-peak residual strength can be realized through the controlled introduction of heterogeneity. In simulations of interfacial fracture within elastically homogeneous materials [4], the probabilistic assignment of element strengths using a normal distribution significantly toughened the interface (relative to results obtained using a uniform assignment of strengths.) Normally distributed strength values allowed for progressive debonding along the interface, whereas uniform strength values led to complete debonding at the critical load.

For further validation, Fig. 19 presents the simulated fracture patterns of specimens with four different internal friction angles (φ = 10°, 20°, 30°, and 40°) within the UCT models. Here, too, the breaking elements are indicated by their corresponding Voronoi cell boundaries. This facilitates the visualization of interior damage development, especially within 3D simulations. The simulated fracture patterns resemble the inclined failure patterns that are typical of the UCT configuration. The broken lines in Fig. 19a–d indicate the critical plane angle, 45° + φ/2, with respect to the horizontal plane. The inclinations of the simulated failure patterns depend on φ and agree well with the theoretical critical planes in all cases.

6. Conclusion

Lattice models provide a simple, effective means for simulating fracture in geomaterials. One ongoing issue, however, has been the inability of lattice models to represent the Poisson effect both macroscopically and in a local sense. The auxiliary stress approach, presented herein, resolves this issue for three-dimensional irregular lattices based on the rigid-body-spring concept. Several conclusions can be made regarding the auxiliary stress approach and its implementation within the lattice model.

1. Both elastic constants (E and ν) are accurately represented, while retaining the simplicity and advantages of using two-node elements. In particular, both global and local representations of the Poisson effect are realized.
2. The lattice model is elastically homogenous: uniform loading of a homogeneous material produces nodal displacements and nodal stresses that agree precisely with theory. Irregular geometry of the lattice does not produce the spurious heterogeneity that is present in conventional lattice models.
3. When simulating basic forms of material heterogeneity, as demonstrated by the example of a stiff inclusion embedded in a homogeneous matrix, the lattice model results compare well with those obtained by the finite element method.
4. Apart from some special cases, described herein, iteration is required to introduce the Poisson effect via the auxiliary stress approach. However, the iterations do not produce a computational burden since they involve only a back-solution of the system equations. The iteration sequence converges more quickly for lower values of Poisson ratio.
5. The proposed approach accommodates the simulation of tensile softening. Uniform fracture energy is consumed along the crack path, in accordance with the prescribed softening relation, without significant bias from the irregular geometry of the lattice. Additional work is needed to extend the approach to accommodate softening behavior under multiaxial loading conditions.
6. Based on physically-derived inputs, the lattice model simulated the split-cylinder test (SCT) and uniaxial compression test (UCT) behaviors of two sets of sedimentary rock samples. In general, the loading branches, peak loads, and failure patterns produced by the model agree well with the experimental results. For the UCT simulations, inclinations of the damage plane are well-defined and in agreement with theory.

Acknowledgements

References

[1] Aoyagi K, Ishii E, Kondo K, Tsusaka K, Fujita T. A study on the strength properties of the rock mass based on triaxial tests conducted at the Horonobe Underground Research Laboratory. Japan Atomic Energy Agency. JAEA-Research 2015-001; 2015.

[2] Asahina D, Houseworth JE, Birkholzer JT, Rutqvist J, Bolander JE. Hydro-mechanical model for wetting/drying and fracture development in geomaterials. Comput Geosci 2014;65:13–23.

[3] Asahina D, Ito K, Houseworth JE, Birkholzer JT, Bolander JE. Simulating the Poisson effect in lattice models of elastic continua. Comput Geotech 2015;70:60–7.

[4] Asahina D, Landis EN, Bolander JE. Modeling of phase interfaces during pre-critical crack growth in concrete. Cem Concr Compos 2011;33(9):966–77.

[5] Bažant ZP, Tabbara MR, Kazemi MT, Pyaudier-Cabot G. Random particle model for fracture of aggregate or fiber composites. J Eng Mech 1990;116 (8):1686–705.

[6] Berton S, Bolander JE. Crack band model of fracture in irregular lattices. Comput Methods Appl Mech Eng 2006;195(52):7172–81.

[7] Bieniawski ZT, Bernede MJ. Suggested methods for determining the uniaxial compressive strength and deformability of rock materials. Int J Rock Mech Min Sci Geomech Abstr 1979;16(2):138–40.

[8] Bolander JE, Moriizumi K, Kunieda M, Yip M. Rigid-Body-Spring Network modeling of cement-based composites. In: The 4th international conference on fracture mechanics of concrete and concrete structures (FraMCoS-4). p. 773–80.

[9] Bolander JE, Saito S. Fracture analyses using spring networks with random geometry. Eng Fract Mech 1998;61(5–6):569–91.

[10] Cho N, Martin CD, Sego DC. A clumped particle model for rock. Int J Rock Mech Min Sci 2007;44(7):997–1010.

[11] Cundall PA. A computer model for simulating progressive large scale movements in blocky rock systems. In: Proceedings of the symposium of the international society rock mechanics.

[12] Cusatis G, Pelessone D, Mencarelli A. Lattice discrete particle model (LDPM) for failure behavior of concrete. I: Theory. Cement Concr Compos 2011;33 (9):881–90.

[13] Cusatis G, Schauffert EA. Discontinuous cell method (DCM) for cohesive fracture propagation. In: The 7th international conference on fracture mechanics of concrete and concrete structures (FraMCoS-7). p. 529–35.

[14] Daw MS, Foiles SM, Baskes MI. The embedded-atom method: a review of theory and applications. Mater Sci Rep 1993;9:251–310.

[15] Grassl P, Fahy C, Gallipoli D, Wheeler SJ. On a 2D hydro-mechanical lattice approach for modelling hydraulic fracture. J Mech Phys Solids 2015;75:104–18.

[16] Griffiths DV, Mustoe GGW. Modelling of elastic continua using a grillage of structural elements based on discrete element concepts. Int J Numer Meth Eng 2001;50(7):1759–75.

[17] Herrmann H, Roux S. Statistical models for the fracture of disordered media (North Holland, Amsterdam, The Netherlands); 1990.

[18] Hondros JR. The evaluation of Poisson's ratio and the modulus of materials of a low tensile resistance by the Brazilian (indirect tension) test with particular reference to concrete. Aust J Appl Sci 1959;10:243–68.

[19] Hori M, Oguni K, Sakaguchi H. Proposal of FEM implemented with particle discretization for analysis of failure phenomena. J Mech Phys Solids 2005;53 (3):681–703.

[20] Ishii E, Funaki H, Tokiwa T, Ota K. Relationship between fault growth mechanism and permeability variations with depth of siliceous mudstones in northern Hokkaido, Japan. J Struct Geol 2010;32(11):1792–805.

[21] Ishii E, Sanada H, Iwatsuki T, Sugita Y, Kurikami H. Mechanical strength of the transition zone at the boundary between opal-A and opal-CT zones in siliceous rocks. Eng Geol 2011;122(3–4):215–21.

[22] ISRM. Suggested methods for determining tensile strength of rock materials. Int J Rock Mech Min Sci Geomech Abstr 1978;15(6):99–103.

[23] ISRM. Suggested methods for determining the strength of rock materials in triaxial compression: revised version. Int J Rock Mech Min Sci Geomech Abstr 1983;20(6):285–90.

[24] Kawai T. New discrete models and their application to seismic response analysis of structures. Nucl Eng Des 1978;48(1):207–29.

[25] Kazerani T, Zhao J. A microstructure-based model to characterize micromechanical parameters controlling compressive and tensile failure in crystallized rock. Rock Mech Rock Eng 2013;47(2):435–52.

[26] Landis EN, Bolander JE. Explicit representation of physical processes in concrete fracture. J Phys D: Appl Phys 2009;42(21):214002.

[27] Monaghan JJ. Smoothed particle hydrodynamics. Ann Rev Astron Astrophys 1992;30:543–74.

[28] Potyondy DO, Cundall PA. A bonded-particle model for rock. Int J Rock Mech Min Sci 2004;41(8):1329–64.

[29] Schlangen E, Garboczi EJ. New method for simulating fracture using an elastically uniform random geometry lattice. Int J Eng Sci 1996;34 (10):1131–44.

[30] Schlangen E, Van Mier JGM. Experimental and numerical analysis of micromechanisms of fracture of cement-based composites. Cem Concr Compos 1992;14:105–18.

[31] Wang G, Al-Ostaz A, Cheng AHD, Mantena PR. Hybrid lattice particle modeling: theoretical considerations for a 2D elastic spring network for dynamic fracture simulations. Comput Mater Sci 2009;44(4):1126–34.

[32] Yip M, Mohle J, Bolander JE. Automated modeling of three-dimensional structural components using irregular lattices. Comput-Aided Civ Infrastruct Eng 2005;20:393–407.

[33] Yoon J. Application of experimental design and optimization to PFC model calibration in uniaxial compression simulation. Int J Rock Mech Min Sci 2007;44(6):871–89.